

# Spectroscopic Modelling of cold ATLASGAL dust Clumps

*Thesis (Phase 1)*

Master of Science

*Submitted by*

**Deepak Chahal**  
(SC18M017)

*Under the guidance of*

**Dr. Jagadheep D.**



Department of Earth and Space Sciences  
(Astronomy & Astrophysics)

Indian Institute of Space Science and Technology  
Thiruvananthapuram, India

July-November 2019



# Certificate

This is to certify that the Thesis (Phase I) titled *Spectroscopic Modelling of cold ATLASGAL dust Clumps* submitted by **Deepak Chahal**, to the Indian Institute of Space Science and Technology, Thiruvananthapuram, in partial fulfillment for the award of the degree of **Master of Science in Astronomy and Astrophysics** is a bona fide record of the original work carried out by him/her under my supervision. The contents of this Thesis (Phase I), in full or in parts, have not been submitted to any other Institute or University for the award of any degree or diploma.

Dr. Jagadheep D.  
Associate Professor

Dr. Samir Mandal  
Head of the Department

**Place:** Thiruvananthapuram

**Date:** November 2019



# Declaration

I declare that this Thesis (Phase I) titled *Spectroscopic Modelling of cold ATLASGAL dust Clumps* submitted in partial fulfillment for the award of the degree of **Master of Science in Astronomy and Astrophysics** is a record of the original work carried out by me under the supervision of **Dr. Jagadheep D.**, and has not formed the basis for the award of any degree, diploma, associateship, fellowship, or other titles in this or any other Institution or University of higher learning. In keeping with the ethical practice in reporting scientific information, due acknowledgments have been made wherever the findings of others have been cited.

**Place:** Thiruvananthapuram  
**Date:** July-November 2019

Deepak Chahal  
(SC18M017)



# Contents

<b>List of Figures</b>	<b>vii</b>
<b>List of Tables</b>	<b>ix</b>
<b>1 Introduction</b>	<b>1</b>
1.1 High Mass Star Formation . . . . .	1
1.2 Motivation of this Study . . . . .	3
<b>2 Methodology</b>	<b>5</b>
2.1 LTE Analysis : for CO and its isotopologues . . . . .	5
2.2 LTE Analysis for two optically thin species . . . . .	9
2.3 Comparison between LTE and RADEX . . . . .	10
<b>3 Data Analysis and Modelling</b>	<b>14</b>
3.1 Observations . . . . .	14
3.2 Analyzing Data for Single Pixel . . . . .	14
3.3 Estimation of H <sub>2</sub> Density . . . . .	24
3.4 Analyzing Data for All Pixels . . . . .	25
<b>4 Results</b>	<b>26</b>
4.1 Integrated Intensity . . . . .	26
4.2 Modelling Results . . . . .	28
<b>5 Future Work</b>	<b>32</b>
<b>Bibliography</b>	<b>32</b>





# List of Figures

2.1	Input and Output parameters of RADEX model . . . . .	11
3.1	An interactive window to display Spectral Cube in GAIA . . . . .	15
3.2	Left and Middle: are two scans in east-west and north-south direction; Right: is the mosaiced scan using WCSMOSAIC . . . . .	16
3.3	Top: $^{12}\text{CO}$ spectra; Middle: $^{13}\text{CO}$ spectra; Bottom: $\text{C}^{18}\text{O}$ spectra, where left is raw spectrum and right is after Hanning smoothing . .	17
3.4	Top-Left: $^{12}\text{CO}$ fitted spectra; Top-Right: $^{13}\text{CO}$ fitted spectra; Bot- tom: $\text{C}^{18}\text{O}$ fitted spectra . . . . .	19
3.5	Functionalities of CASSIS . . . . .	20
3.6	Left: CO modelled with optimized fit; Right: CO spectra modelled with LTE obtained temp 25 K . . . . .	22
3.7	Offset in Spectra for several pixels of $\text{C}^{18}\text{O}$ compared $^{13}\text{CO}$ . . . . .	24
4.1	Integrated intensity ( $\text{K kms}^{-1}$ ) maps for $^{12}\text{CO}$ (top-), $^{13}\text{CO}$ (middle) and $\text{C}^{18}\text{O}$ (bottom) . . . . .	27
4.2	Spectrum of CO showing blue-shifted and red-shifted wings . . . . .	28
4.3	Integrated intensity map of CO plotted with blue and red contours corresponding to blue-shifted and red-shifted wings respectively . . .	28
4.4	Column Density ( $\text{cm}^{-2}$ ) map of $^{13}\text{CO}$ . . . . .	29
4.5	Column density map of $\text{C}^{18}\text{O}$ . . . . .	30
4.6	Excitation temperature map of $^{13}\text{CO}$ . . . . .	30
4.7	Velocity wrt LSR map of $^{13}\text{CO}$ . . . . .	31
4.8	Observed isotopic ratio [ $^{13}\text{CO}/\text{C}^{18}\text{O}$ ] . . . . .	31



# List of Tables

1.1	ATLASGAL sources targeted in the Study . . . . .	4
2.1	List of RADEX input and output parameter values for different molecules	11
2.2	Constants for different molecules . . . . .	12
2.3	Input parameters used and corresponding output results from LTE Model	12
3.1	Average signal to ratio for three scans . . . . .	16
3.2	Number of Channels hanned and their corresponding S/N ratio . . .	18
3.3	Fitted parameters of CO and its isotopologues . . . . .	18
3.4	List of parameters required to model a single component and molecule and obtained beam efficiency . . . . .	22
3.5	List of parameters required to model a single component and molecule by varying size and the obtained optimum size of source . . . . .	23



# Chapter 1

## Introduction

### 1.1 High Mass Star Formation

Molecular clouds are both the coldest and densest regions of the interstellar medium (ISM), and are the sites of star formation. The number density of molecular hydrogen in these structures range from few hundred  $\text{cm}^{-3}$  in molecular clouds up to  $\approx 10^6 \text{ cm}^{-3}$  in the dense cores where star formation happens. The study of the early stages of star formation can be carried out from observations of the dense clumps and cores which are unstable against gravitational collapse. Molecular line and dust continuum emission in the submillimeter are among the main tools to study these initial stages of massive star formation, where the sources are still deeply embedded in the molecular gas. (Afonso et al., 1998) The complexity of the molecular line emission process can be exploited to tell us about the physical properties of molecular clouds. In addition Molecular line measurements can also provide the kinematics of the dense gas to probe systematic motions in the dense core such as infall, outflows, rotation etc as long as the observed species is reasonably abundant. (Lee et al., 2007)

Several properties of these deeply embedded cores are still an enigma, such as flows of high velocity molecular gas observed from regions of active star formation. These flows are now recognized as supersonic outflows dispersing remnant gas and dust from the core contributing to the overall stability of the cloud. Presence of these high velocity gases are evidence that the core is in early stage of star formation. Though several observational studies of such outflows has been done but there is no clear understanding of origin of the energy and momentum driving the flows. (Girart et al., 1999) These proto-stellar outflows can dynamically compress the surrounding gas and adjacent dense cores, and promote fragmentation and gravitational contraction leading to star formation. (Shimajiri et al. 2008), (Nakamura et al., 2019)

Although molecular hydrogen ( $\text{H}_2$ ) is the most dominant component in molecular clouds, it cannot be observed directly.  $\text{H}_2$  molecule being homonuclear has no permanent dipole moment, dipole transitions ( $\Delta J = 1$ ) are forbidden. The allowed rotational transitions are quadrupole transitions which have low emissivity. (Krumholz, 2011) Also moment of inertia of  $\text{H}_2$  is small, its first rotational transition ( $J = 2 - 0$ ) at  $28.2 \mu\text{m}$  is therefore at a relatively high temperature ( $h\nu/k \approx 508 \text{ K}$ ), for which minimum gas temperature of  $T_k \approx 150 \text{ K}$  is required for appreciable collisional excitation. So several trace molecules such as  $\text{CO}$ ,  $\text{HCN}$ ,  $\text{N}_2\text{H}^+$  and  $\text{HCO}^+$  which have higher dipole moments, and their larger moment of inertia leads to lowest rotational transitions at millimeter wavelengths ( $90 - 115 \text{ GHz}$  typically), corresponding to  $h/k$  of a few K. (Scoville, 2012) While the rotational lines are often optically thick, the molecular isotopologues such as  $^{13}\text{CO}$ ,  $\text{C}^{18}\text{O}$ ,  $\text{H}^{13}\text{CO}^+$ ,  $\text{H}^{13}\text{CN}$  etc are optically thin and can be used to probe dense regions.

A molecular line's sensitivity to gas density depends on its critical density,  $n_{crit}$ , the density at which the collisional excitation and radiative de-excitation rates are equal. For densities higher than the critical density, the excitation is dominated by collisions, and the level populations come into equilibrium with the gas kinetic temperature (i.e.,  $T_{ex} = T_{kin}$ ). For smaller values of density, radiative processes dominate and the level populations come in equilibrium with the temperature of the radiation field,  $T_{rad}$  (i.e.,  $T_{ex} = T_{rad}$ ). For molecular clouds that are well shielded from the diffuse interstellar radiation field, the background radiation is typically the Cosmic Microwave Background ( $T_{rad} = 2.73 \text{ K}$ ) while the kinetic temperature is around  $10 \text{ K}$ . Since the line brightness is essentially proportional to the excitation temperature, molecular emission lines become strong only when collisions dominate, i.e., when the gas density exceeds the critical density. (Goldsmith, 1999) The critical densities of rotational transitions is proportional to  $\mu^2 \nu_{J+1,J}^3$  (for optically thin lines at frequency  $\nu_{J+1,J}$ ). Since the dipole moment of  $\text{CO}$  is low ( $0.112 \text{ D}$ ), the critical density is also low  $\sim 300 \text{ cm}^{-3}$ . Hence  $\text{CO}$  is excited by both high density gas in dense cores and lower density gas in the overall cloud. For this reason,  $\text{CO}$  is often used to study the overall cloud structure rather than the denser cores. The  $\text{CO}$  emission will trace the overall distribution of  $\text{H}_2$  for densities  $n_{\text{H}_2} \approx 10^{2-3} \text{ cm}^{-3}$ . (Klessen, 2011)

From the measurements of rare  $^{13}\text{C}$  isotopologues of both  $\text{CO}$  and  $\text{HCN}$ , it was found that the intensity of the isotopologues is approximately 0.1-0.5 times of the abundant species whereas the ISM abundance ratio is  $^{13}\text{C}/\text{C} = 1/89 - 1/40$ . This implies that the emission from the abundant species is optically thick and is therefore satu-

rated. (Scoville, 2012) CO condenses out onto dust grain surfaces at low temperatures preventing us from observing the high density structures from where signature of collapse can be evident. This can be clearly seen from the comparison of maps made in the millimeter dust continuum with maps of CO. High velocity wings are often seen in CO spectra along the dense regions, which are evidence of outflowing gas driven by the core. Since CO is optically thin at these wings, a good estimate of outflow properties can be made from CO spectrum. (Shimoikura et al., 2015)

HCN ( $J = 1-0$ ) and  $\text{HCO}^+$  ( $J = 1-0$ ) molecular transitions have critical densities  $n_{crit} \approx 3 \times 10^6 \text{ cm}^{-3}$  and  $2 \times 10^5 \text{ cm}^{-3}$  due to their higher dipole moments and therefore higher A-coefficients. Hence they are a probe of higher density molecular gas compared to CO. HCN has been used routinely as an infall tracer in low-mass starless cores and also in high-mass star-forming regions. (Goicoechea et al., 2019)  $\text{N}_2\text{H}^+$  is another tracer of high density gas since it is known to be a selective tracer of quiescent gas, it is particularly suitable for studying the structure and kinematics of cold star forming cores. (Caselli et al., 2002) Being an ion,  $\text{N}_2\text{H}^+$  is also important to trace the ionized gas and provides information about the coupling between ions and neutrals in high density cores which are in early stages of star formation

## 1.2 Motivation of this Study

The process of high mass star formation is still poorly understood and there is no general theory about their formation and evolution as in case of low-mass star formation. Observational studies of high-mass star formation also pose significant challenges. This is due to the short formation time-scale, enhancement of hydrogen burning before the accretion of gas has stopped, clustered environment for their formation and the rarity and large distances to regions of active high-mass star formation. The evolution of massive stars also affect the surrounding parent cloud due to stellar winds, massive outflows, strong UV radiation, and expansion of HII regions. (Goicoechea et al., 2019) These strong impacts alter the physical conditions and chemical composition of the cloud and can even cause contraction, triggering the formation of a new generation of stars. Since high-mass stars always form in clusters, the whole cluster potential has to be taken into account to study different pre-evolutionary stages of star formation.

The primary aim of this project is to study a sample of dense clumps selected from the ATLASGAL survey which are in early stages of high mass star formation,

**Table 1.1:** ATLASGAL sources targeted in the Study

S.N.	Name	$\alpha$ (J2000) (h,m,s)	$\delta$ (J2000) ( $^{\circ}$ ' ")	$S_P$ at 870 $\mu\text{m}$ (Jy/beam)	$V_{LSR}$ (km/s)
1	AG 36.899-00.409	19:00:08.48	03:20:35.70	0.93	80
2	AG 36.794-00.204	18:59:13.11	03:20:36.80	0.69	78.1
3	AG 36.826-00.039	18:58:41.31	03:26:49.60	0.64	60.2
4	AG 41.049-00.247	19:07:12.48	07:06:19.30	1.05	66
5	AG 41.077-00.124	19:06:49.15	07:11:14.10	0.65	63.3
6	AG 46.174-00.524	19:17:49.80	11:31:07.50	0.8	50.1
7	AG 46.426-00.237	19:17:16.48	11:52:30.50	0.94	52.3
8	AG 47.031-00.244	19:16:41.18	12:38:05.90	0.95	54.9
9	AG 47.051-00.251	19:16:42.03	12:39:20.70	1.19	56
10	AG 49.253-00.411	19:23:21.22	14:17:22.10	1.16	66.1

to understand their physical properties and kinematics using molecular spectroscopy. Since different molecular transitions traces different physical properties of the clumps, this project aims to model the spectra for several molecules such as  $^{12}\text{CO}$ ,  $^{13}\text{CO}$ ,  $\text{C}^{18}\text{O}$  and high density gas tracers  $\text{HCO}^+$ ,  $\text{H}^{13}\text{CO}^+$ ,  $\text{HCN}$  and  $\text{N}_2\text{H}^+$ . The details of the sources are shown in the Table 1.1. In addition to the ATLASGAL names of the sources and equatorial coordinates, the table also list the peak ATLASGAL (870  $\mu\text{m}$ ) fluxes ( $S_P$ ). Study has been carried out till now only on one clump which is AG 36.899-00.409.

This thesis is organized as follows. Chapter 2 describes the methodology goes behind in the calculation of several parameters like excitation temperature, column density etc that are required to study the physical properties of these clumps. It also contains comparison of numerical estimates of parameters derived from two approaches : LTE (Local Thermodynamic Equilibrium) and non-LTE. Chapter 3 includes the description of the data and how the modelling of spectroscopic lines for  $^{12}\text{CO}$ ,  $^{13}\text{CO}$  and  $\text{C}^{18}\text{O}$  have been performed using GILDAS and CASSIS. Chapter 4 describes the results obtained from modelling, and a brief discussion on the subsequent work that needs to be performed.



## Chapter 2

# Methodology

Ideally, one needs observations of multiple transition of a molecule, in order to estimate excitation temperature and column density. For observations of a single transition of a molecule, the most common approach is simply to assume Local Thermodynamic Equilibrium (LTE) , which is equivalent to saying that all energy levels are populated according to a Boltzmann distribution at a single temperature, which is the kinetic temperature of the gas,  $T_{kin}$  .

The excitation temperature, which is close to the kinetic temperature if the density is significantly above the critical density, can be estimated if the transition is optically thick. If the transition is optically thin, the column density can be estimated by assuming a value for the excitation temperature. If the observations of an optically thick transition of a molecule and an optically thin transition of an isotopologue are available, both quantities can be estimated by assuming the excitation temperature to be same for the molecule and its isotopologue.

### 2.1 LTE Analysis : for CO and its isotopologues

Since CO is the second most abundant molecule after  $H_2$ , the molecule and its isotopologues are useful to trace the overall structure of the cloud. Due to its higher abundance it can be assumed to be in thermal equilibrium with its isotopologues. So an estimate of the excitation temperature can be done using CO molecular transition as it is optically thick, and the column density can be estimated from its isotopologues under the assumption of LTE. (Liu et al., 2014)

### 2.1.1 Excitation Temperature

The excitation temperature is defined as the temperature required to give the relative populations of the upper and lower levels in accordance with the Boltzmann equation

$$\frac{n_J}{n_{J-1}} = \frac{g_J}{g_{J-1}} e^{-E_{J,J-1}/kT_{ex}} \quad (2.1)$$

where  $E_{J,J-1}$  is the energy of rotational transition between rotational state  $J$  and  $J-1$ ,  $n_J$  and  $n_{J-1}$  are the number densities in upper and lower level respectively, and  $g_J$ ,  $g_{J-1}$  are the degeneracies corresponding to levels  $J$  and  $J-1$ .

The radiative transfer equation is given by :

$$\frac{dI_\nu}{ds} = -\alpha_\nu I_\nu + j_\nu \quad (2.2)$$

where  $I_\nu$  is the specific intensity,  $j_\nu$  is the emission co-efficient and  $\alpha_\nu$  is the absorption co-efficient. The equation above can be written in terms of the optical depth and source function as

$$\frac{dI_\nu}{d\tau} = -I_\nu + S_\nu \quad (2.3)$$

where  $S_\nu = j_\nu/\alpha_\nu$  is the source function. For thermal emission, the source function is equal to the blackbody function,  $B_o(T)$ . If the source function is a constant in the medium, the solution to eq. (2.3) is

$$I_\nu(\tau_\nu) = I_\nu(0)e^{-\tau_\nu} + S_\nu(1 - e^{-\tau_\nu}) \quad (2.4)$$

where  $I_\nu(0)$  is the background intensity. In a typical observation, two observations are taken, one on the source wherein the intensity received is as per eq. (2.4) above, and another off the source where the intensity is received is equal to the background intensity,  $I_\nu(0)$ . Subtracting the "on" and "off" spectra, one gets

$$I_\nu(\tau_\nu) - I_\nu(0) = [S_\nu - I_\nu(0)] (1 - e^{-\tau_\nu}) \quad (2.5)$$

Since the  $J = 3-2$   $^{12}\text{CO}$ ,  $^{13}\text{CO}$  and  $\text{C}^{18}\text{O}$  occur at 345, 330 and 329 GHz respectively and the temperature of molecular clouds is typically from 10 to 20 K, one can assume Rayleigh Jeans approximation for these transitions. Then, the specific intensity is

related to the observed Main beam temperature by

$$I_\nu = \frac{2k\nu^2}{c^2} T_{MB} \quad (2.6)$$

Substituting eq. (2.6) into eq. (2.5) above, one gets (Phillips et al., 1979)

$$T_{MB} = \eta \frac{h\nu}{k_B} \left[ \frac{1}{e^{h\nu/kT_{ex}} - 1} - \frac{1}{e^{h\nu/kT_{bg}} - 1} \right] (1 - e^{-\tau_\nu}) \quad (2.7)$$

where  $T_{ex}$  is the excitation temperature for the molecule. Under the assumption of LTE, one can assume that  $^{12}\text{CO}$ ,  $^{13}\text{CO}$  and  $\text{C}^{18}\text{O}$  will have the same excitation temperature. The background temperature  $T_{bg}$  is assumed to be the Cosmic Microwave Background in case of molecular clouds. In eq. (2.7),  $\eta$  is the beam filling factor which indicates the fraction of the beam that is filled by the source. If the source size,  $\theta_s$ , is known, the beam filling factor can be estimated as

$$\eta = \frac{\theta_s^2}{\theta_s^2 + \theta_b^2} \quad (2.8)$$

where  $\theta_b$  is the beam size of the telescope. Since CO is optically thick in almost all dense cloud cores,  $1 - e^{-\tau} \approx 1$  and eq. (2.7) becomes (Paron et al., 2018; Polychroni et al., 2012; Padoan et al., 1997)

$$T_{ex} = \frac{h\nu}{k_B} \frac{1}{\left[ \log \left( \frac{\eta h\nu}{k_B [T_{MB} + J(T_{bg})]} + 1 \right) \right]} \quad (2.9)$$

where  $J(T_{bg})$  is as per eq. (2.10)

$$J(T) = \frac{h\nu}{k_B} \frac{1}{(e^{h\nu/k_B T} - 1)} \quad (2.10)$$

Eq. (2.9) can be used to estimate the excitation temperature from the observed properties of the CO line.

## 2.1.2 Column Density

The first step to estimate column density is to determine the optical depth of optically thin isotopologues. Since all isotopologues have same excitation temperature, one can use eq. (2.7) to get an estimate of Optical depth ( $\tau_\nu$ ), from the observed main beam

temperature of  $^{13}\text{CO}$  and  $\text{C}^{18}\text{O}$ . (Padoan et al., 1997)

$$\tau(^{13}\text{CO}) = -\log \left( 1 - \frac{T_{MB}(^{13}\text{CO})}{\eta [J(T_{ex}) - J(T_{bg})]} \right) \quad (2.11)$$

To get the column density from the optical depth, recall that the absorption coefficient can be written in terms of the Einstein coefficients as :

$$\alpha_\nu = \frac{h\nu}{4\pi} \phi(\nu) [n_{J-1}B_{J-1,J} - n_J B_{J,J-1}] \quad (2.12)$$

The Einstein B-coefficients are related according to eq. (2.13)

$$g_{J-1}B_{J-1,J} = g_J B_{J,J-1} \quad (2.13)$$

while  $n_{J-1}$  and  $n_J$  are related by eq. (2.1). For a Gaussian line shape, the profile function is given by

$$\phi(\nu) = \sqrt{\frac{4 \log 2}{\pi}} \frac{1}{\Delta v} e^{-(v-v_o)^2 4 \log 2 / \Delta v^2} \quad (2.14)$$

where  $\Delta v$  is the full width at half-maximum (FWHM) line width. Then, the value of absorption coefficient at line center ( $v = v_o$ ) is (Padoan et al., 1997)

$$\alpha_\nu = \sqrt{\frac{\ln 2}{4\pi^3}} \frac{hc}{\Delta v} n_J B_{J,J-1} (e^{\Delta E/kT_{ex}} - 1) \quad (2.15)$$

Integrating the absorption coefficient over the line of sight, one gets :

$$\tau_\nu = \int \alpha_\nu ds = \sqrt{\frac{\ln 2}{4\pi^3}} \frac{hc}{\Delta v} B_{J,J-1} (e^{\Delta E/kT_{ex}} - 1) \int n_J ds \quad (2.16)$$

Integrating the number density of upper level over the line of sight will yield the column density of the upper level ( $N_J$ ). In case of a linear molecule each state can be labelled by its rotational quantum number  $J$ , with corresponding energy  $E_J$  being given by  $hB_o J(J+1)$  (where  $B_o$  is the rotational constant of the molecule). The frequency for the rotational transition ( $J-1$ ) given by  $\nu_{J,J-1} = 2B_o J$  (Goldsmith, 1972) and the Einstein B-coefficient corresponding to the transition is (Goldsmith and Langer, 1999) :

$$B_{J,J-1} = \frac{8\pi^3 \mu^2}{3h^2} \frac{J}{J+1} \quad (2.17)$$

where  $\mu$  is the permanent electric dipole moment for the molecule. Substituting eq. (2.17) in eq. (2.16) and re-arranging the terms gives the Column density as

$$N_J = \frac{3}{16\sqrt{\pi^5 \ln 2}} \frac{h\Delta v}{\mu^2} \left( \frac{2J+1}{J} \right) \frac{\tau_\nu}{(e^{\Delta E/kT_{ex}} - 1)} \quad (2.18)$$

For a molecule in LTE, since the excitation temperature is the same for all energy levels, the population of each level is given by

$$N_J = \frac{N}{Z} g_J e^{-E_J/kT_{ex}} \quad (2.19)$$

where  $N$  is the total column density of the species and  $Z$  is partition function given by

$$Z = \sum_i g_i e^{-E_i/kT} \quad (2.20)$$

In the limit where  $kT \gg hB_o$ , the summation can be approximated as an integral using the substitution  $u = J(J+1)$  (Goldsmith and Langer, 1999):

$$Z = \sum_{J=0}^{J=\infty} (2J+1) e^{-hB_o J(J+1)/kT} \rightarrow \int_0^\infty e^{-au} du = a^{-1} = kT/hB_o \quad (2.21)$$

Substituting eqs. (2.19),(2.20),(2.21) in eq. (2.18), one obtains the total column density as :

$$N = \frac{3}{16\sqrt{\pi^5 \log 2}} \frac{\Delta v k T_{ex}}{J \mu^2 B_o} \frac{e^{J(J+1)hB_o/kT_{ex}}}{(e^{2B_o Jh/kT_{ex}} - 1)} \tau_\nu \quad (2.22)$$

## 2.2 LTE Analysis for two optically thin species

For the case of the two isotopologues where neither transition is optically thick, another approach can be used to derive excitation temperature if both molecules are optically thin. An example of this case are the  $\text{HCO}^+$  and  $\text{H}^{13}\text{CO}^+$  molecules which are generally observed to be optically thin. In this case,  $(1 - e^{-\tau} \approx \tau)$  (Girart et al., 1999) and taking the ratio of eq. (2.7) for both the molecules (in the below equation  $\text{HCO}^+$  and  $\text{H}^{13}\text{CO}^+$  is referred as 12 and 13 in subscript respectively) :

$$\frac{T_{MB_{12}}}{T_{MB_{13}}} = \left[ \frac{J_{\nu_{12}}(T_{ex}) - J_{\nu_{12}}(T_{bg})}{J_{\nu_{12}}(T_{ex}) - J_{\nu_{13}}(T_{bg})} \right] \frac{\tau_{12}}{\tau_{13}} \quad (2.23)$$

where  $J(T)$  is expressed in eq. (2.10). Taking the ratios of column densities of both molecules from eq. (2.22) and rearranging the terms gives the ratio of optical depths as :

$$\frac{\tau_{12}}{\tau_{13}} = \frac{(NJ\mu^2 B_o)_{12}}{(NJ\mu^2 B_o)_{13}} \frac{\Delta v_{13}}{\Delta v_{12}} \left[ \frac{(e^{2B_o J h / k T_{ex}} - 1)_{12}}{(e^{2B_o J h / k T_{ex}} - 1)_{13}} \right] \left[ e^{(J(J+1)h B_o / k T_{ex})_{13} - (J(J+1)h B_o / k T_{ex})_{12}} \right] \quad (2.24)$$

Using eq. (2.23) and (2.24), an estimate of the excitation temperature can be obtained if one assumes the ratio of column densities of  $\text{HCO}^+$  and  $\text{H}^{13}\text{CO}^+$  to be equal to the ratio of  $^{12}\text{C}$  to  $^{13}\text{C}$  which is estimated to be 50-100. Dickman (1976); Rigby et al. (2015); Milam et al. (2005) An analytical expression for  $T_{ex}$  can be obtained if one assumes  $J(T_{bg})$  to be negligible in comparison to  $J(T_{ex})$  for both the molecules :

$$T_{ex} = \frac{h [J_{12}(J_{12} + 1)B_{12} - J_{13}(J_{13} + 1)B_{13}]}{k \left( \log \left[ \frac{(B\nu\mu^2)_{12}}{(B\nu\mu^2)_{13}} \frac{(\Delta v T_{MB})_{13}}{(\Delta v T_{MB})_{12}} \left[ \frac{^{12}\text{CO}}{^{13}\text{CO}} \right] \right] \right)} \quad (2.25)$$

Once the excitation temperature is known, the optical depth and column density can be estimated using eqs. (2.11) and (2.22) respectively.

## 2.3 Comparison between LTE and RADEX

In practical scenario, it is not always possible that the molecule and its isotopologues are in thermal equilibrium. So to understand any kind of discrepancy in the output parameters with the assumption of LTE model, a comparison of parameters such as column density , excitation temperature etc has been carried out between LTE and non-LTE models. Both the models require different input and provide different output parameters which are described further.

### 2.3.1 RADEX : Non-LTE Model

RADEX is a radiative transfer model code, which incorporates the effect of collisional excitation from different molecules in the molecular cloud. It provides a constraint on physical conditions such as density, kinetic temperature etc to analyze the large set of observational data. It uses escape probability formulation with an assumption of isothermal and homogeneous medium. (Van der Tak et al., 2007) This model requires  $\text{H}_2$  density to incorporate the effect of collisional excitation. The model

takes the column density of the molecule ( $N$ ), line width ( $\Delta v$ ), kinetic temperature ( $T_{kin}$ ) and  $H_2$  density ( $n_{H_2}$ ) as an input and calculate the optical depth ( $\tau$ ), excitation temperature ( $T_{ex}$ ) and corresponding main beam temperature ( $T_{MB}$ ). The approach of RADEX runs in reverse compared to LTE where main beam temperature gives excitation temperature and corresponding column density. Fig. 2.1 lists the various input parameters required for RADEX as an input and also the corresponding output parameters generated from the model.

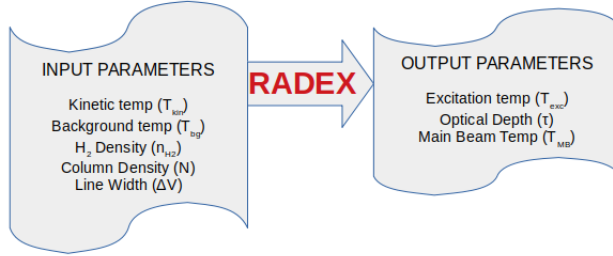


**Figure 2.1:** Input and Output parameters of RADEX model

The input parameters have been given the typically observed values for ( $J = 1 - 0$ ) molecular transition. Since the critical density of CO and its isotopologues is lower, which suggest that it traces less dense gas, so  $H_2$  density is kept lower ( $\approx 10^3 \text{ cm}^{-3}$ ). While critical density is higher in case of  $HCO^+$  and its isotopologues, considered as a dense gas tracer, corresponding  $H_2$  density is set higher ( $\approx 10^5 \text{ cm}^{-3}$ ). Background temperature ( $T_{bg}$ ) and line width ( $\Delta v$ ) are kept same i.e 2.73 K and 1 km/s respectively for all the molecules. Typically observed value for column densities have been given for  $^{12}\text{CO}$ ,  $^{13}\text{CO}$ ,  $\text{C}^{18}\text{O}$  (Rigby et al., 2015) and  $HCO^+$ ,  $H^{13}\text{CO}^+$  Shimoikura et al. (2015) as mentioned in the Table 2.1. Obtained output parameters with the corresponding input for each molecule are listed in the Table 2.1

**Table 2.1:** List of RADEX input and output parameter values for different molecules

Molecules	INPUT					OUTPUT		
	$T_{kin}$ (K)	$T_{bg}$ (K)	$n_{H_2}$ ( $\text{cm}^{-3}$ )	$N$ ( $\text{cm}^{-2}$ )	$\Delta v$ (km/s)	$T_{ex}$ (K)	$\tau$	$T_{MB}$
CO	20	2.73	$10^3$	$5 \times 10^{16}$	1	14.318	4.753	10.8
$^{13}\text{CO}$	20	2.73	$10^3$	$5 \times 10^{14}$	1	9.039	0.1005	0.55
$\text{C}^{18}\text{O}$	20	2.73	$10^3$	$1 \times 10^{14}$	1	8.899	0.0261	0.114
$HCO^+$	30	2.73	$10^5$	$5 \times 10^{12}$	1	10.558	0.642	1.982
$H^{13}\text{CO}^+$	30	2.73	$10^5$	$5 \times 10^{10}$	1	10.751	0.0052	0.0233

### 2.3.2 LTE Model

An analysis to calculate excitation temperature and column density from main beam temperature has been already discussed for CO and its isotopologues in section (2.1), and in section (2.2) for HCO<sup>+</sup> and H<sup>13</sup>CO<sup>+</sup>. The input parameters required to perform the desired LTE calculations are background temperature ( $T_{bg}$ ), line width ( $\Delta v$ ) and frequency of transition which are kept same as that in RADEX, referred from section (2.3.1). And the main beam temperature for LTE has been taken to be the output main beam temperature from RADEX, mentioned in Table 2.1. The estimate of excitation temperature and column density requires various constants such as frequency of transition, rotational constant, dipole moment etc which are listed in Table 2.2 for each molecule. Column density for CO has been derived from <sup>13</sup>CO by considering a ratio of [CO/<sup>13</sup>CO] = 70. (Wilson and Rood, 1994)

**Table 2.2:** Constants for different molecules

Molecules	Frequency ( $J = 1 - 0$ )(GHz)	Rotational Constant $B_o$ (GHz)	Dipole Moment $\mu$ (Debye)
<sup>13</sup> CO	110.201	55.101	0.11046
C <sup>18</sup> O	109.782	54.891	0.11049
HCO <sup>+</sup>	356.734	44.594	3.88
H <sup>13</sup> CO <sup>+</sup>	346.998	43.377	3.9

Derived output results from LTE approach have been listed in Table 2.3, for both cases i.e CO and its isotopologues using section (2.1), and also for two optically thin species which are HCO<sup>+</sup> and H<sup>13</sup>CO<sup>+</sup> using section (2.2). For CO optical depth is assumed to be very high ( $\tau \gg 1$ ), so no mentioned in Table 2.3.

**Table 2.3:** Input parameters used and corresponding output results from LTE Model

Molecules	INPUT			OUTPUT		
	$T_{MB}$ (K)	$T_{bg}$ (K)	$\Delta v$ (km/s)	$T_{ex}$ (K)	$\tau$	N (cm <sup>-2</sup> )
CO	10.8	2.73	1	14.27	-	$4 \times 10^{16}$
<sup>13</sup> CO	0.55	2.73	1	14.27	0.0482	$5.75 \times 10^{14}$
C <sup>18</sup> O	0.114	2.73	1	14.27	0.00979	$1.19 \times 10^{14}$
HCO <sup>+</sup>	1.982	2.73	1	10.558	0.806	$1.11 \times 10^{13}$
H <sup>13</sup> CO <sup>+</sup>	0.0233	2.73	1	10.751	0.00917	$1.21 \times 10^{11}$



### 2.3.3 Conclusion

A comparison between the derived output results from LTE and non-LTE (RADEX) models has been drawn. Optical depth of CO from RADEX results in 4.75, so an assumption of considering CO to be optically thick is valid. Excitation temperature derived using LTE model is 14.27 K which is same as derived from RADEX. Though excitation temperature and optical depth for  $^{13}\text{CO}$  and  $\text{C}^{18}\text{O}$  derived from LTE model are slight different but the order of magnitude is similar to RADEX. Column densities derived from LTE model are almost same as that in RADEX for CO and its isotopologues. So LTE assumption of considering same excitation temperature of  $^{13}\text{CO}$  and  $\text{C}^{18}\text{O}$  is justifiable.

In case of LTE model for two optically thin molecules, derived excitation temperature is 8.3 K while 10.5 K in RADEX model. Even optical depth for both the molecules are of similar order compared with RADEX model. So not much discrepancy has been observed in excitation temperature and optical depth. Though the optical depth of  $\text{HCO}^+$  is 0.645, which certainly donot makes it optically thin. But the estimation of column density also have similar order of magnitude from both the models. So the assumption of  $\text{HCO}^+$  being optically thin and both isotopologues are in thermal equilibrium is legitimate.

If one consider the LTE approach for the estimation of column density and excitation temperature, the order of magnitude is same as that from non-LTE (RADEX). So all assumptions for LTE are valid, so these assumptions will not create a higher order discrepancy in estimation.

## Chapter 3

# Data Analysis and Modelling

### 3.1 Observations

The sources were selected from the ATLASGAL survey (Schuller et al., 2009) at 870  $\mu\text{m}$  to study the fragmentation properties at high resolution. The sources were selected to be in an early evolutionary stage based on clump averaged emission at 24  $\mu\text{m}$  in the MIPS GAL survey (Carey et al., 2009). The sources were observed with the 15m James Clark Maxwell Telescope (JCMT) in order to study and characterize the physical conditions and kinematics of the dense clumps. The observations were carried using the Heterodyne Array Receiver Program (HARP) which has 16 single sideband (SSB) receivers in a  $4 \times 4$  configuration that can be tuned between 325 and 375 GHz. The HARP receiver array was used with the ACSIS digital autocorrelation spectrometer backend which was typically configured to have two 250 GHz subbands with 4096 channels each. The configuration allows one to observe certain combinations of spectral lines such as  $^{13}\text{CO}$  and  $\text{C}^{18}\text{O}$  simultaneously.

The 10 ATLASGAL sources were mapped in several molecules such as  $^{12}\text{CO}$ ,  $^{13}\text{CO}$ ,  $\text{C}^{18}\text{O}$ ,  $\text{HCO}^+$ ,  $\text{H}^{13}\text{CO}^+$ ,  $\text{HCN}$  and  $\text{N}_2\text{H}^+$ , and targeted observations were taken for weaker spectral lines such as methanol. The mapping observations were done with two on-the-fly mapping scans, one in the east-west direction and the other in the north-south direction.

### 3.2 Analyzing Data for Single Pixel

The raw data were reduced using standard pipeline, with the pipeline reduced data being available in the JCMT archive. The reduced data were in the form of spectral

cubes. The data were inspected using the GAIA toolkit that is part of the STARLINK package [<http://starlink.eao.hawaii.edu/starlink>], screenshot of which is shown in Fig 3.1 where cross refers to the position of pixel whose spectra has been displayed.

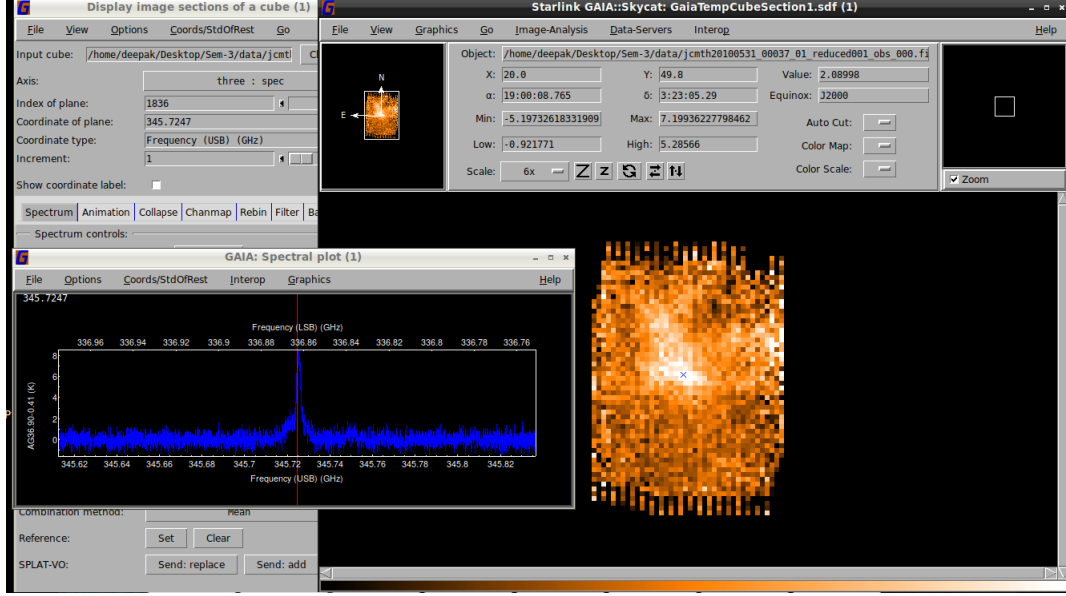


**Figure 3.1:** An interactive window to display Spectral Cube in GAIA

### 3.2.1 Averaging two Scans

Since two maps made from scans in orthogonal directions are available, a weighted average of these scans can achieve a better S/N ratio. This can be done in the STARLINK package using the task WCSMOSAIC, which aligns and rebins a group of input maps into a single output map as per their WCS co-ordinates. The data were first loaded into STARLINK into its native format (called NDF) and were then aligned and averaged using WCSMOSAIC. Fig 3.2 shows the individual scan maps and the output after mosaicing. The mosaiced data were checked to ensure that the intensity of the output maps were consistent with these provided as input. It was also observed that the signal to noise ratio improved upon mosaicing as expected as shown in Table 3.1.

### 3.2.2 Modifying the Axes

The data obtained from the JCMT archive uses the barycentric frame of reference for the frequencies (and velocities). This needs to be transferred to the local standard of

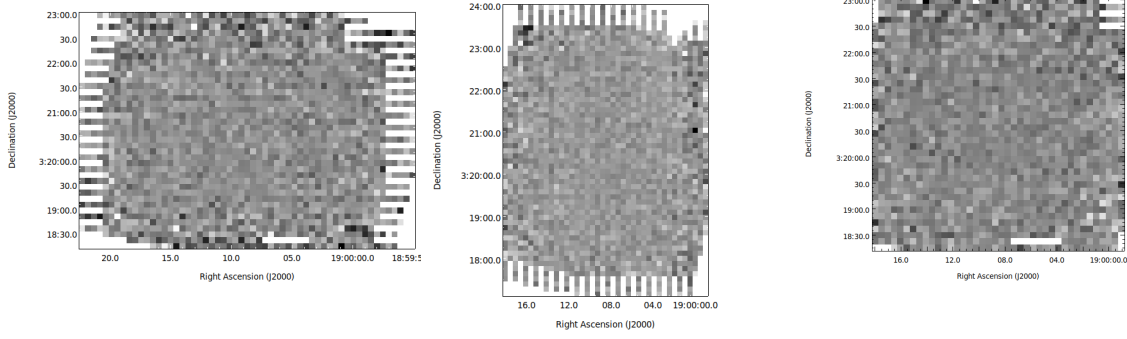


**Figure 3.2:** Left and Middle: are two scans in east-west and north-south direction; Right: is the mosaiced scan using WCSMOSAIC

**Table 3.1:** Average signal to ratio for three scans

Signal to Noise (S/N)		
SCAN 1	SCAN 2	WCSMOSAIC
12.47	12.52	13.89

rest (LSR) frame of reference. This is done by applying eq. (3.1) where (10.3, 15.3, 7.7) are  $(u, v, w)$  velocity components of Sun wrt to LSR frame of reference and  $l, b$  are galactic longitude and latitude respectively.

$$V_{LSR} = V_{bary} + (10.3 \cos l + 15.3 \sin l) \cos b - 7.7 \sin b \quad (3.1)$$

An additional problem encountered in CLASS (a part of the GILDAS package) was that the map co-ordinates were not read properly. This was traced to a few FITS keywords used by the STARLINK pipeline which were not standard. For instance, the keywords which govern the change in co-ordinate value for right ascension, declination and spectral frequency are CDELTA1, CDELTA2 and CDELTA3 respectively. The pipeline processing of STARLINK gave the keywords as CD1, CD2 and CD3 which were not recognized by GILDAS software [<https://www.iram.fr/IRAMFR/GILDAS/>]. These were fixed manually by editing the header.

### 3.2.3 Smoothing and Fitting

To model the spectral cube using radiative transfer, one requires estimates of parameters like line width, LSR velocity corresponding to the line, and peak antenna

temperature. To obtain this information, we loaded the data into GILDAS software and fit the lines using the CLASS package. To work with spectra, fits file was first converted into lmv (data cube format for GILDAS) using the VECTOR command and then to a malt file, which is the CLASS default extension.

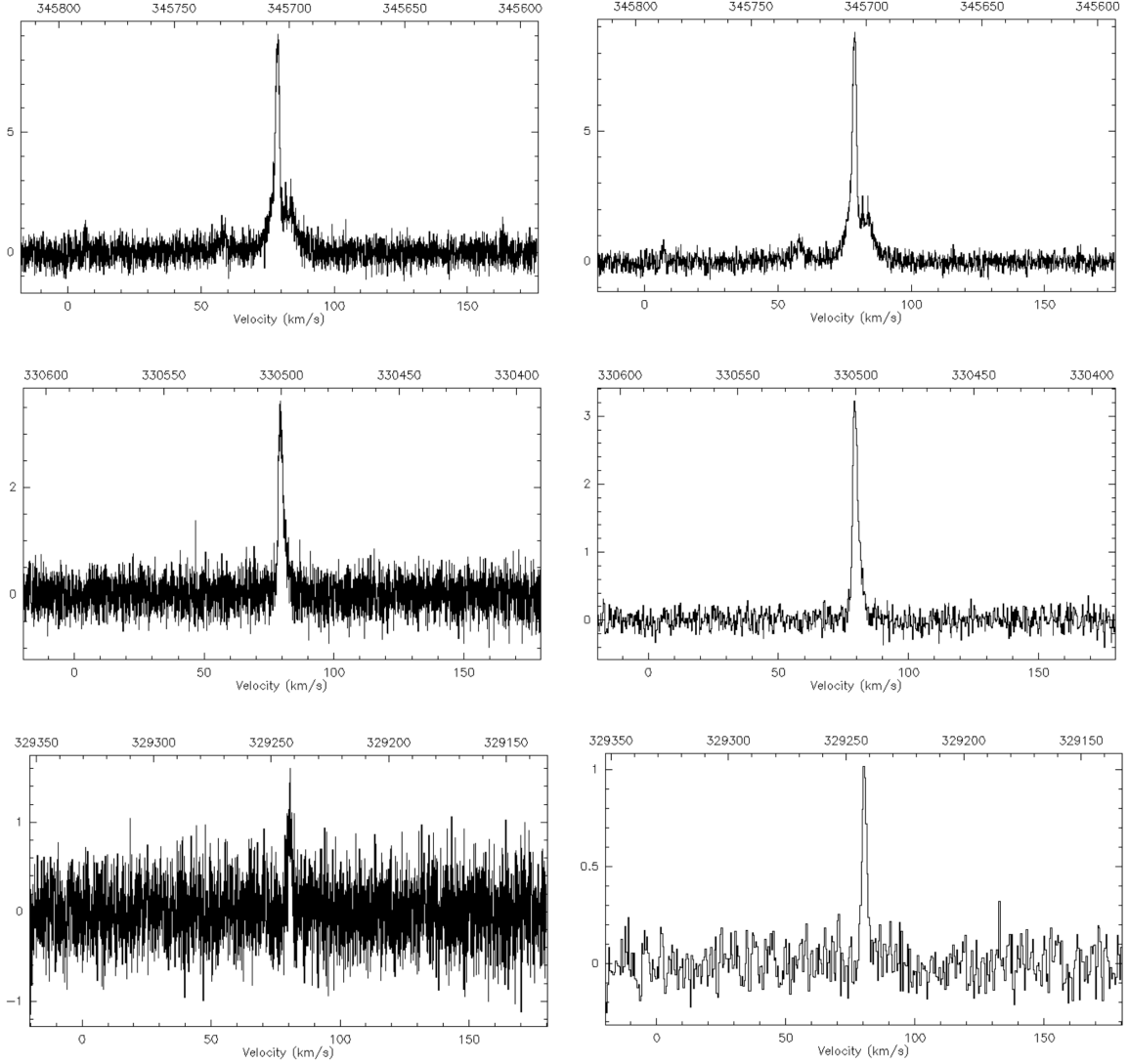


**Figure 3.3:** Top:  $^{12}\text{CO}$  spectra; Middle:  $^{13}\text{CO}$  spectra; Bottom:  $\text{C}^{18}\text{O}$  spectra, where left is raw spectrum and right is after Hanning smoothing

### 3.2.3.1 Smoothing the Spectra

The native spectra of  $^{13}\text{CO}$  and  $\text{C}^{18}\text{O}$  are at very high velocity resolution (0.0553 km/s) and have significant noise compared to signal. Hence, the spectra are smoothed

**Table 3.2:** Number of Channels hanned and their corresponding S/N ratio

Molecules	Before HANNING		After HANNING		
	Velocity Resolution (km/s)	S/N	No. of Channels smoothed	Velocity Resolution (km/s)	S/N
CO	0.0553	12.059	2	0.1106	19.28
<sup>13</sup> CO	0.0553	4.506	4	0.2212	10.96
C <sup>18</sup> O	0.0553	1.172	8	0.4424	4.008

by Hanning smoothing in CLASS to improve the signal to noise ratio. The <sup>12</sup>CO, <sup>13</sup>CO and C<sup>18</sup>O data are smoothed to a velocity resolution of 0.1106, 0.2212 and 0.4424 km/s respectively based on the signal to noise ratio consideration. Examples of spectra before and after are shown in Fig. 3.3 and their corresponding signal to noise ratio before and after hanning is shown in Table 3.2.

### 3.2.3.2 Fitting the Spectra

To fit the data, first step is baseline subtraction which can be done using low order polynomial. We used a zero order polynomial since the baselines are close to being flat, after pipeline processing. After baseline subtraction, Gaussian fit can be done by specifying velocity range containing the line. For <sup>12</sup>CO and <sup>13</sup>CO molecules simultaneous Gaussian fitting with two components has been performed while a single Gaussian fit. has been used in case of C<sup>18</sup>O as can be seen in Fig 3.4. For CO molecule, broad velocity component (line width  $\cong$  10 km/s) is required to fit the spectra properly due to the presence of blue-shifted and red-shifted wings in CO spectra. The fit parameters of a sample spectrum of each isotopologue is shown in Table 3.3 and the fit spectra are shown in Fig 3.4.

**Table 3.3:** Fitted parameters of CO and its isotopologues

Molecules	Component	Peak (K)	Position (km/s)	Linewidth (km/s)	RMS (K)
CO	1	10.51	78.65	1.64	0.522
	2	2.98	80.01	10.94	
<sup>13</sup> CO	1	4.41	79.20	1.46	0.393
	2	2.02	80.80	3.33	
C <sup>18</sup> O	1	1.70	80.50	2.22	0.297

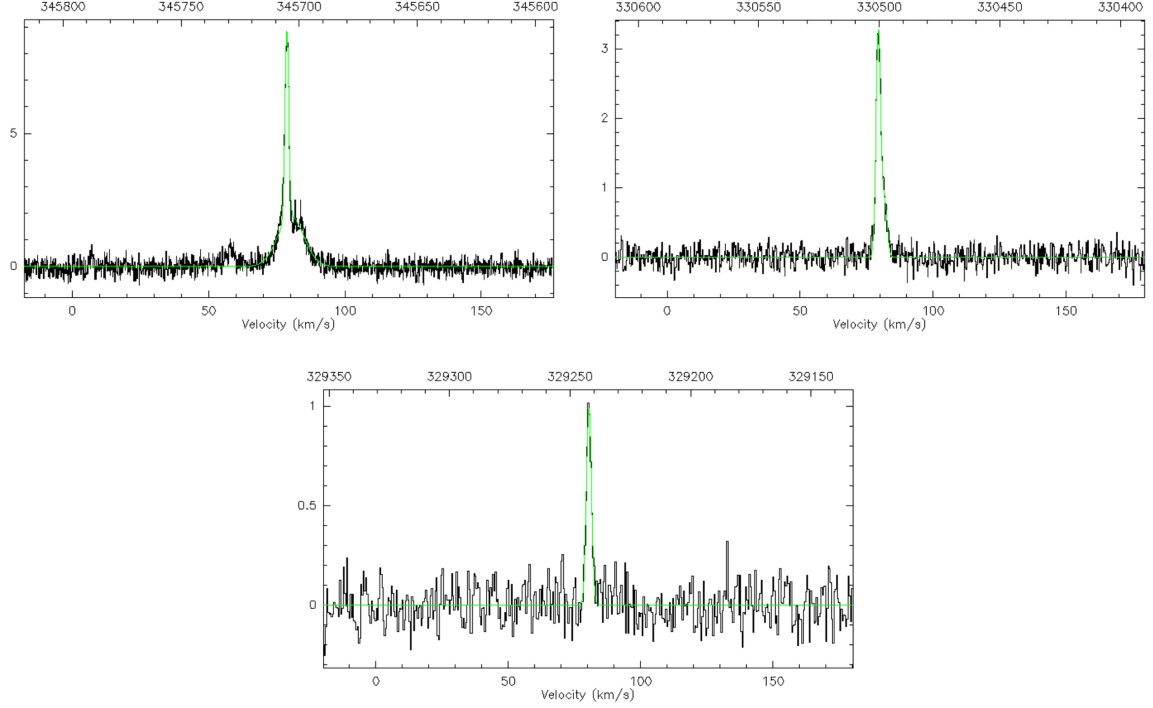


**Figure 3.4:** Top-Left:  $^{12}\text{CO}$  fitted spectra; Top-Right:  $^{13}\text{CO}$  fitted spectra; Bottom:  $\text{C}^{18}\text{O}$  fitted spectra

### 3.2.4 Radiative Transfer Modelling using CASSIS

CASSIS (Centre d'Analyse Scientifique de Spectres Infrarouges et Submillimétriques) [<http://cassis.irap.omp.eu/?page=cassis>] is a software package aimed for scientific analysis of high resolution observations. It uses local spectroscopic database combining the JPL and CDMS molecular spectroscopic databases, and the atomic spectroscopic database NIST. Tools available for modelling the astrophysical objects are LTE and RADEX connected to LAMDA molecular collisional database as shown in Fig 3.5. CASSIS mainly requires column density, line width, excitation temperature and model the line by calculating optical depth and main beam temperature. To search through the parameter space for optimum fit, it simplifies the search for best physical parameters for modelling an astrophysical source using a regular grid or a Markov chain Monte Carlo (MCMC) methods. Modelling can be done manually in a interactive mode and also through LineAnalysis scripting using which range and initial guess for the parameters can be set. Varying the range and initial guess for the parameters helps in achieving a better fit and provides optimum results.

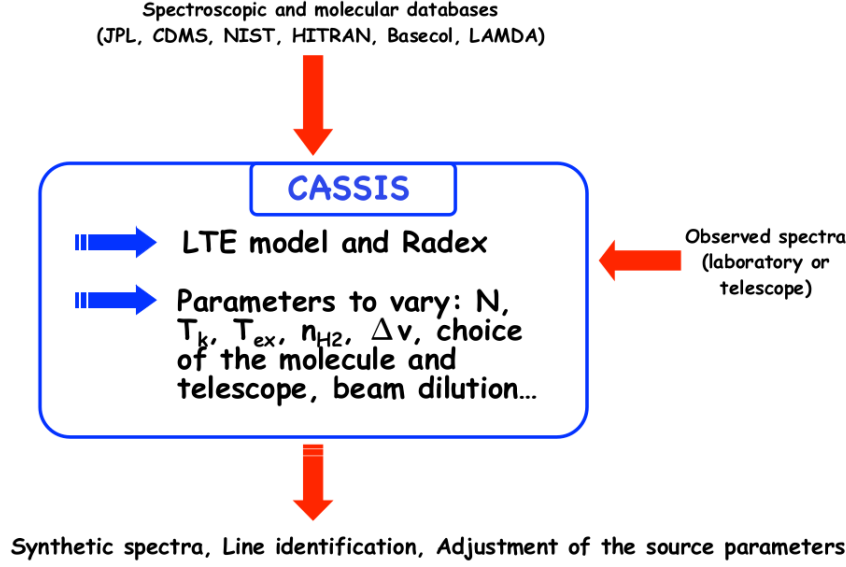


Figure 3.5: Functionalities of CASSIS

#### 3.2.4.1 Parameters for Modelling

Before modelling the spectra, a thorough understanding of different parameters required for modelling in CASSIS, so that the correct range and initial guess can be set to obtain an optimum model.

1. *Column Density* : An estimate of molecular column density is made from the RADEX, by running it for different column densities to achieve the desired main beam temperature.
2. *Excitation Temperature* : An average range for excitation temperature in molecular clumps is 10-30 K, so initial guess for modelling has been done with a range of 20-30 K.
3. *LSR Velocity* : which is the velocity in local standard of rest corresponding to the molecular line, has been estimated from the Gaussian fit in CLASS as mentioned in Table 3.3.
4. *FWHM* : is the full width half maximum of the spectral line need to be modelled. An estimate of range of the FWHM for both single and multiple components has also been carried out from the fitted spectra in CLASS as mentioned in Table 3.3.



5. *Size* : Size of the source is required for the estimation of beam dilution factor (as mentioned in section 2.1.1). If the size of source doesnot fill the beam, it reduces the main beam temperature. So to get beam averaged output results, size of the source is given as the size of beam ( $\simeq 14.7''$ ).
6. *Iso* : is the Isotopic ratio, this parameter is useful while modelling two molecules simultaneously. CASSIS will optimize the model for second molecule by just varying the column density. It will be useful when two molecules are in local thermal equilibrium as this is the case with CO and its isotopologues.
7. *Interacting/Non-Interacting* : CASSIS provides a tool to restrict the interaction between the different components. Interaction will modify the intensity of radiation coming from the inner component due to optical depth of outer component.
8. *LTE/RADEX* : CASSIS provides two approach for modelling the spectra : LTE and Non-LTE (RADEX), both of which have been already discussed in Chapter 2.

#### 3.2.4.2 CASSIS Modelling

Data has been corrected to main beam temperature using main beam efficiency ( $\eta_{Beff}=0.64$ )[<https://www.eaobservatory.org/jcmt/instrumentation/heterodyne/harp/>]. Two components have been used to model CO, but to obtain more optimum results it requires three components. CO has been modelled with three components but to achieve an optimum fit as shown in the left spectra of Fig 3.6, excitation temperature required is  $\approx 90$ -100 K. While to fit for same main beam temperature using LTE model gives 25 K. Fig. 3.6 shows the right spectrum which is modelled with temp of 25 K obtained from LTE model. So such low temperature is saturating the fit, higher temperatures are required to achieve optimum fit. Column density is also coming higher  $\simeq 2 \times 10^{17} \text{cm}^{-2}$ , while  $4 \times 10^{16} \text{cm}^{-2}$  from LTE model. To analyze this discrepancy, modelling for a single component and molecule has been performed without optimization.

1. *Main Beam Efficiency* : is the percentage of received power which enters the main beam. Main beam temperature has been measured at different excitation temperature and column density. It has been found that all the main beam temperatures are lower by a factor of 0.55 compared to theoretical LTE model

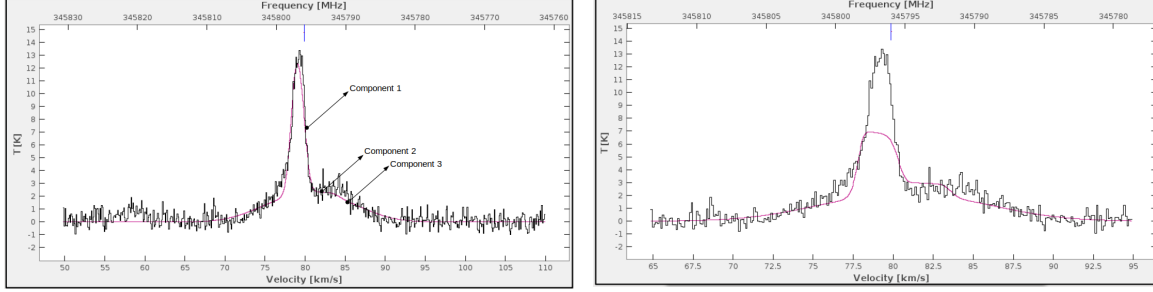


**Figure 3.6:** Left: CO modelled with optimized fit; Right: CO spectra modelled with LTE obtained temp 25 K

as shown in Table 3.4. It shows that the CASSIS is by default changing the Main Beam temperature to Antenna temperature. To use newly calibrated value for beam efficiency (0.64),  $T_{MB}2T_A$  is set to FALSE which will allow CASSIS to model with Main beam temperature only.

**Table 3.4:** List of parameters required to model a single component and molecule and obtained beam efficiency

S.N.	N ( $\text{cm}^{-2}$ )	$T_{ex}$ (K)	$T_{MB}$ (K) CASSIS	$T_{MB}$ (K) LTE	$\eta_{Beff}$
1	$10^{16}$	40	5.676	10.35	0.55
2	$10^{17}$	40	17.64	31.64	
3	$10^{18}$	40	17.43	31.7	
4	$10^{16}$	70	5.34	9.72	
5	$10^{17}$	70	27.91	50.74	
6	$10^{18}$	70	34.37	62.68	

2. *Beam Dilution Factor* : To obtain a beam averaged column densities, size of source has been set same as beam size ( $1.22\lambda/D_{tel} = 14.7''$ ). To understand the effect of size on modelled parameters, size has been varied keeping other parameters constant as shown in Table 3.4. Lower main beam temperature has been observed for lower size of source compare to LTE model, while for higher size main beam temperature tends towards LTE model can be seen in Table 3.5. A size of source much greater than beam size provides same values of main beam temperature as in LTE model. So a Beam Dilution factor as mentioned in eq. (2.8) multiplies to the Main beam temperature and reduces it further.

For a source filling the beam size, size of source should be much higher than beam size.

**Table 3.5:** List of parameters required to model a single component and molecule by varying size and the obtained optimum size of source

S.N.	SIZE (")	N (cm <sup>-2</sup> )	T <sub>ex</sub> (K)	T <sub>MB</sub> (K) CASSIS	T <sub>MB</sub> (K) LTE	$\theta_s^2/(\theta_s^2 + \theta_b^2)$
1	10	10 <sup>17</sup>	40	10.03	32.36	0.31
2	40	10 <sup>17</sup>	40	27.84	31.64	0.88
3	80	10 <sup>17</sup>	40	30.97	31.93	0.97
4	1000	10 <sup>17</sup>	40	32.4	32.1	1.01

### 3.2.4.3 Simultaneous Modelling

Corrected for the main beam efficiency (0.64) and the size of the source has been set to much greater than the beam size i.e ( $\approx 1000''$ ). CASSIS allows one to model two molecules simultaneously using parameter isotopic ratio. Two molecules should be in thermal equilibrium to get model simultaneously, since CASSIS fit with the same excitation temperature, line width for second molecule by just varying column density to obtain optimum fit.

1. <sup>12</sup>CO-<sup>13</sup>CO : <sup>13</sup>CO has been modelled simultaneously with <sup>12</sup>CO, by providing isotopic ratio (50-90) (Polychroni et al., 2012) with three components. The broader component ( $\simeq 10$ km/s) is not present in <sup>13</sup>CO, giving lower abundance ratio compared to what is generally observed. Setting interaction between components, also yields similar results. A true estimate of parameters cannot be done by modelling with CO. Even modelling C<sup>18</sup>O with <sup>12</sup>CO also provides higher values. It is possible that the broader component is creating such discrepancy from theoretical LTE model.
2. <sup>13</sup>CO-C<sup>18</sup>O : It has been observed that the spectra of both <sup>13</sup>CO and C<sup>18</sup>O shows consistency as both can be easily fit with two components. Output parameters shows promising results when compared with theoretical LTE model, but a shift in the C<sup>18</sup>O spectra has been observed from <sup>13</sup>CO spectra which leads to a non-optimum fit. Another problem is that the isotopic ratio is coming at lower side i.e 3-5, while generally observed is [<sup>13</sup>CO/C<sup>18</sup>O] $\approx$  7-10. (Wilson and Rood, 1994; Goldsmith and Langer, 1999)

- *Offset in  $C^{18}O$*  : While modelling  $^{13}CO$  with  $C^{18}O$ , an offset in spectra of both molecules has been observed. Similar kind of offset have been observed in several other pixels between  $C^{18}O$  and  $^{13}CO$ . By analyzing several pixels an average offset in spectra has been found to be  $0.5 \text{ kms}^{-1}$  as shown in the Fig 3.7. So to model the two molecules together, the spectra of  $C^{18}O$  has been shifted by  $0.5 \text{ kms}^{-1}$  for all pixels.

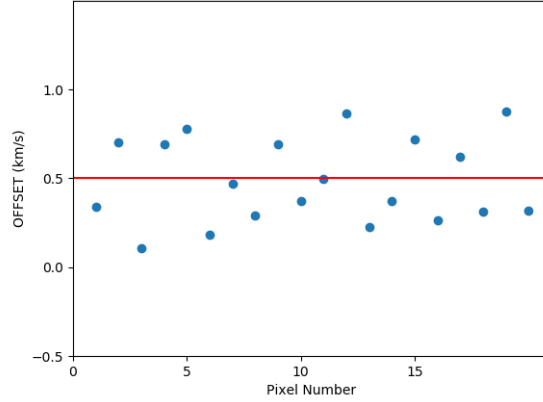


**Figure 3.7:** Offset in Spectra for several pixels of  $C^{18}O$  compared  $^{13}CO$

### 3.3 Estimation of $H_2$ Density

An estimation of  $H_2$  column density can be made from the ATLASGAL  $870 \mu\text{m}$  dust emission map. Given flux density for each pixel can be converted into specific intensity. Considering background as negligible compared to source function and dust emission to be optically thin, eq. (2.4) reduces to eq. (3.2), where  $B_\nu$  is the planck function,  $I_\nu$  is specific intensity and  $\tau$  is optical depth :

$$I_\nu = B_\nu(T)(1 - e^{-\tau}) = B_\nu(T)\tau \quad (3.2)$$

$\tau_\nu = \int \alpha_\nu ds = \int \kappa_\nu \rho ds$  , where  $\kappa_\nu$  is dust opacity assumed to be  $1.85 \text{ cm}^2/\text{g}$  [Ossenkopf and Henning (1994)],  $\rho$  is density of dust. Ratio of density of  $H_2$  and density of dust is generally found to be 100 (Paron et al., 2018). Substituting these expressions in eq. (3.2) and multiply-divide by the mass of single atom ( $\mu m_H$ ) to get the

H<sub>2</sub> column density in eq. (3.2).

$$I_\nu = B_\nu(T)\kappa\mu m_H \int \frac{\rho ds}{\mu m_H} = B_\nu(T)\kappa\mu m_H N_{H_2} \quad (3.3)$$

where  $m_H$  is the Hydrogen mass,  $\mu = 2.8$  by adopting a relative mass fraction of 0.7 for H<sub>2</sub> (Paron et al., 2018). Taking a dust temperature from ATLASGAL 870  $\mu\text{m}$  (Schuller et al., 2009), obtained H<sub>2</sub> column density  $N_{H_2} = 2.2 \times 10^{22} \text{cm}^{-2}$

## 3.4 Analyzing Data for All Pixels

Modelling for one pixel has been discussed till now, modelling for whole pixel space  $40 \times 59$  has been performed. Several pixels with bad signal to noise ratios have been masked.

### 3.4.1 Smoothing and Fitting the Data

A *for* loop was run in CLASS to perform multiple task for each spectra such as setting offset, baseline subtraction with zero degree polynomial and fitting the spectrum with Gaussian profile. Noisy pixels have been masked using an *If* condition in the *for* loop. Masked out pixels were having  $S/N < 3\sigma_{RMS}$  and  $1 > \delta v$ ,  $\delta v > 4$ . Pixels with good S/N ratios are stored with their fitted parameters in a text file.

### 3.4.2 Modelling the Data

A *for* loop script in the shell terminal provides one the opportunity to run CLASS and CASSIS consecutively. Setting up a script containing *for* loop, which generate spectrum from the CLASS and model it in CASSIS. Output modelled parameters saved in a text file are extracted to create maps of excitation temperature, line width, LSR velocity and column density.

# Chapter 4

## Results

Base on the signal to noise consideration, total of  $40 \times 59$  pixels were modelled in  $^{13}\text{CO}$  and  $\text{C}^{18}\text{O}$ . The  $^{12}\text{CO}$  spectra were not modelled due to the presence of the line wings.

### 4.1 Integrated Intensity

The integrated intensity maps for  $^{12}\text{CO}$ ,  $^{13}\text{CO}$  and  $\text{C}^{18}\text{O}$  has been generated by integrating the spectral line profile over the velocity range of emission and are shown in Fig 4.1. It is clearly evident that the integrated intensity peaks of  $^{12}\text{CO}$  is much higher than  $^{13}\text{CO}$  and  $\text{C}^{18}\text{O}$ . The integrated intensity maps shows two peaks at  $(\alpha, \delta) \equiv (19^{\text{h}} 00^{\text{m}} 08^{\text{s}}, 03^{\circ} 20' 40'')$  and  $(19^{\text{h}} 00^{\text{m}} 12^{\text{s}}, 03^{\circ} 21' 10'')$ . It is also evident that  $^{12}\text{CO}$  can be seen at various places of the cloud which is not visible in case of  $^{13}\text{CO}$  and  $\text{C}^{18}\text{O}$ . In contrast,  $\text{C}^{18}\text{O}$  emission is visible only in the central region.

#### 4.1.1 Outflows in CO map

Fig. 4.2 shows a typical  $^{12}\text{CO}$  spectrum in the observed region. The spectrum shows a broad component which would trace an outflow from the central core. To check the presence of outflows, integrated intensity maps of both blue-shifted and red-shifted wings has been made. With the velocity ranges  $76 > V_{\text{LSR}} > 72$  km/s and  $88 > V_{\text{LSR}} > 84.5$  km/s being considered for the blue and red shifted wings respectively. Fig 4.3 shows map of blue and red wings in blue and red contours superimposed on the integrated intensity map. A clear spatial separation between the peak integrated intensity map is evident between the two wings which strongly suggest the presence of an outflow.(Shimoikura et al., 2015) It can also be seen that the red-shifted wing shows higher integrated intensity compared with the blue-shifted one.

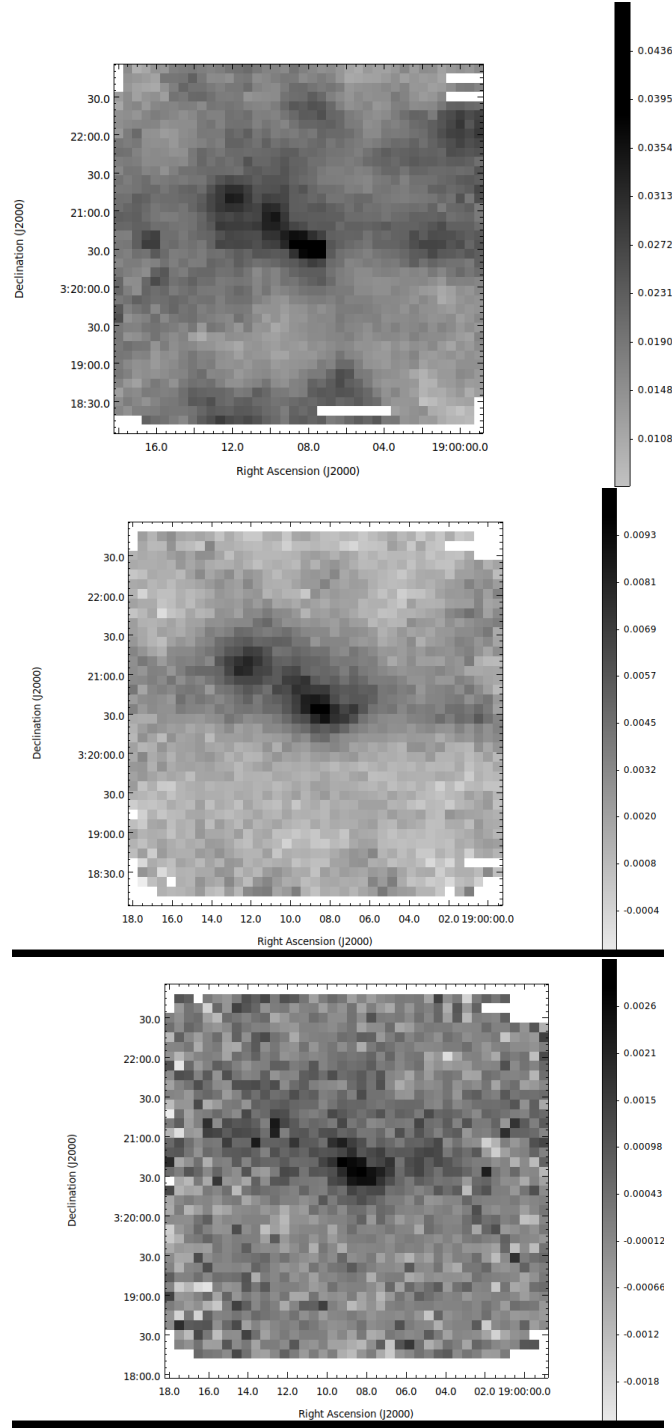


**Figure 4.1:** Integrated intensity (K kms<sup>-1</sup>) maps for <sup>12</sup>CO (top-), <sup>13</sup>CO (middle) and C<sup>18</sup>O (bottom)

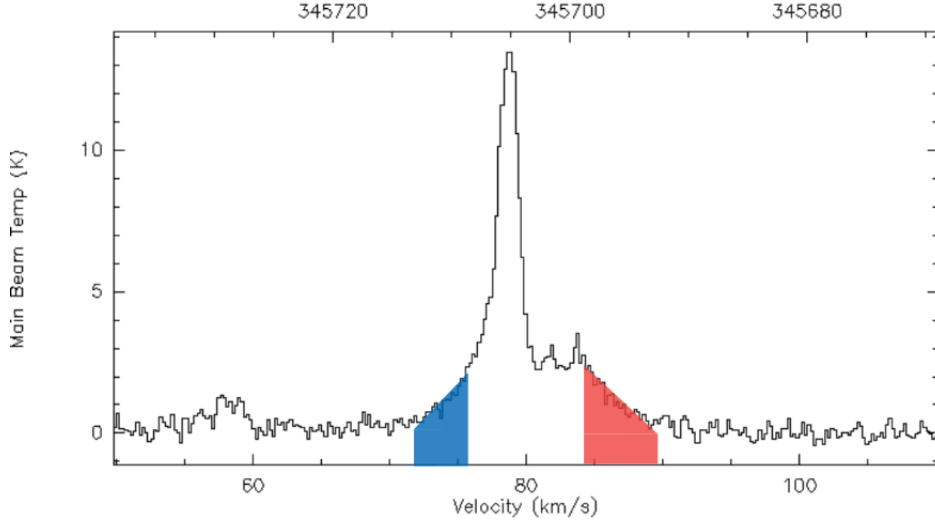


**Figure 4.2:** Spectrum of CO showing blue-shifted and red-shifted wings

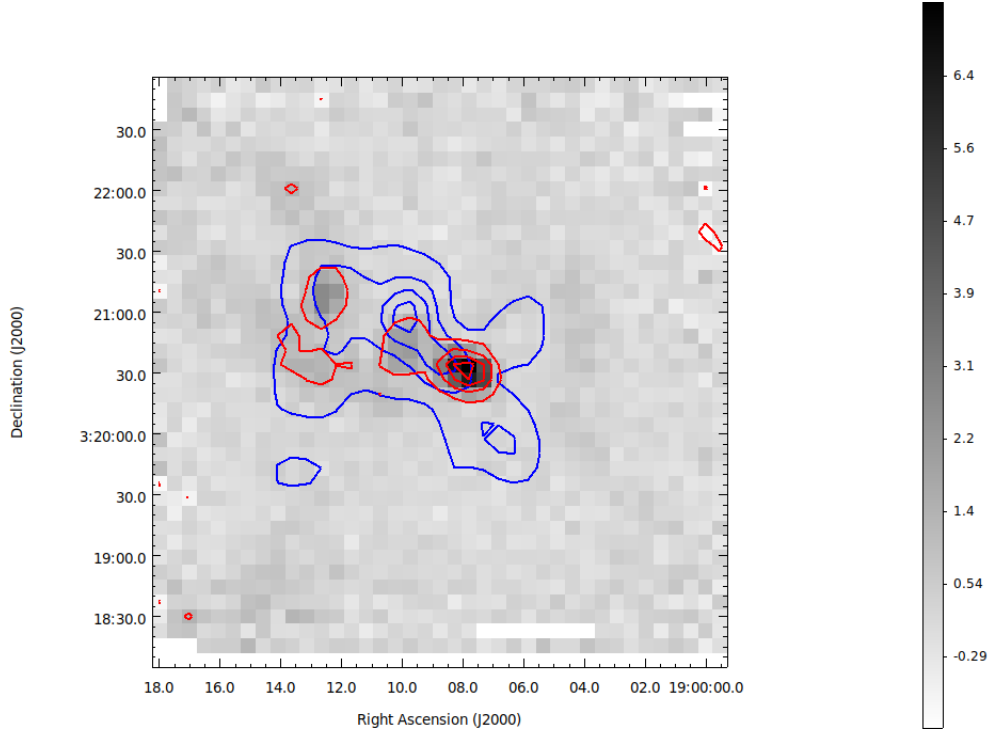


**Figure 4.3:** Integrated intensity map of CO plotted with blue and red contours corresponding to blue-shifted and red-shifted wings respectively

## 4.2 Modelling Results

### 4.2.1 Column Density

Fig. 4.4 shows the total  $^{13}\text{CO}$  column density derived by simultaneous modelling of  $^{13}\text{CO}$  and  $\text{C}^{18}\text{O}$  using CASSIS.



It can be seen that the column density of  $^{13}\text{CO}$  traces a morphology similar to that of the total integrated intensity, with the peak column density being measure towards first core at  $(\alpha, \delta) \equiv (19^{\text{h}} 00^{\text{m}} 08^{\text{s}}, 03^{\circ} 20' 40'')$ . Core 1 shows a peak column density of  $5.86 \times 10^{15} \text{ cm}^{-2}$ , while core 2 shows slightly lower peak column density of  $5.2 \times 10^{15} \text{ cm}^{-2}$ . When considered with the peak column density of molecular hydrogen  $2.2 \times 10^{22} \text{ cm}^{-2}$  as measured from the  $800 \mu\text{m}$  ATLASGAL dust emission map, this shows the abundance of  $^{13}\text{CO}$  to be  $[^{13}\text{CO}/\text{H}_2] 2.6 \times 10^{-7}$ . Considering typical  $[^{12}\text{C}/^{13}\text{C}] \approx 70$  and  $X[^{12}\text{CO}/\text{H}_2] \approx 10^{-5}$  (Wilson and Rood, 1994; Goldsmith and Langer, 1999) provides an abundance ratio for  $^{13}\text{CO} \approx 1.4 \times 10^{-7}$ , which is almost similar to what we have found. Emission from core 1 are also traced by  $\text{C}^{18}\text{O}$  column density map as can be seen in Fig. 4.5

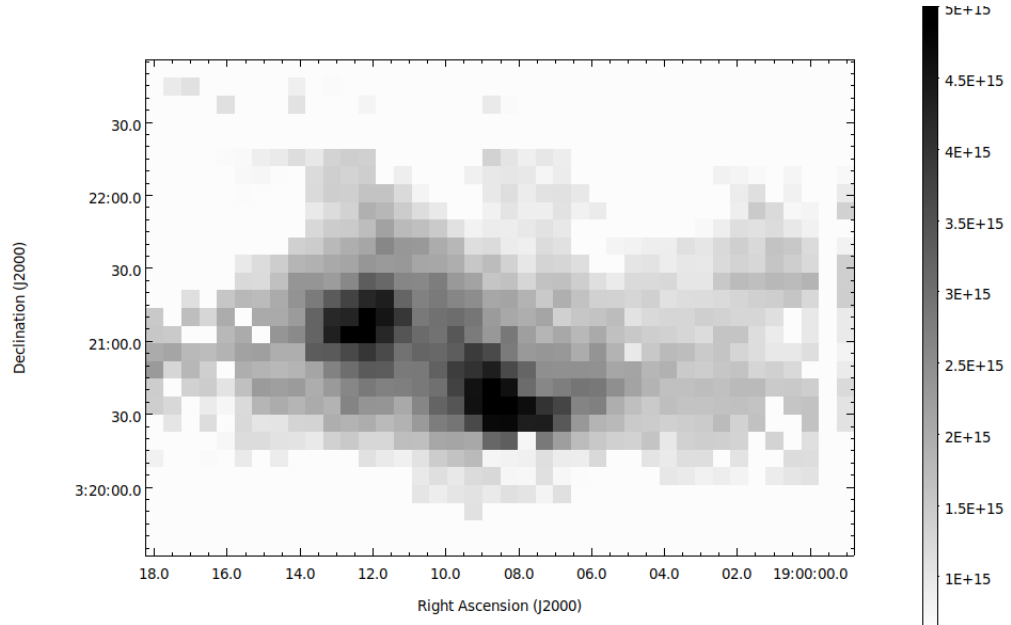


**Figure 4.4:** Column Density ( $\text{cm}^{-2}$ ) map of  $^{13}\text{CO}$

## 4.2.2 Excitation Temperature

The left panel of Fig. 4.6 shows the map of excitation temperature in the region. The excitation temperature ranges from 25-37 K. The excitation temperature is seem to be more or less uniform in the region which suggest that the gas traced by  $^{13}\text{CO}$  is close to being isothermal.

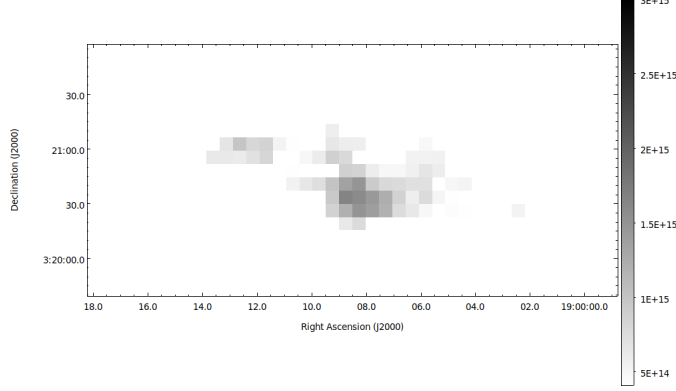


**Figure 4.5:** Column density map of  $\text{C}^{18}\text{O}$

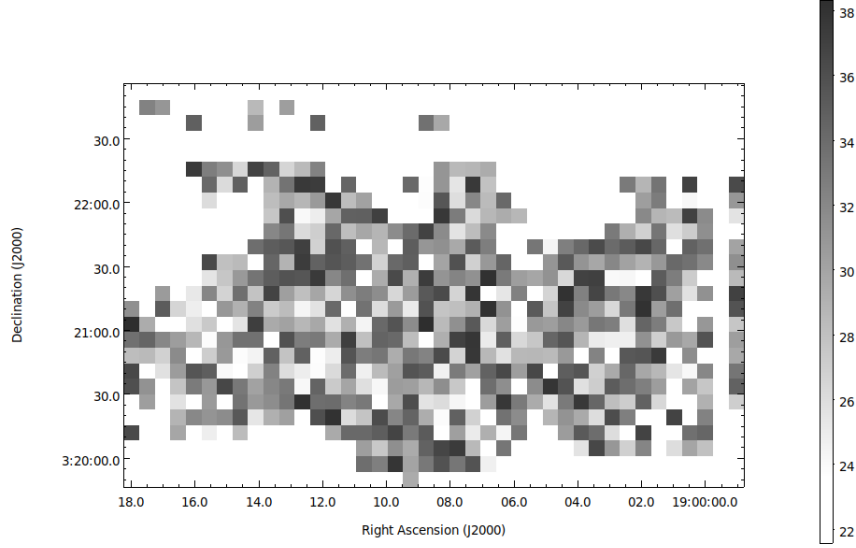


**Figure 4.6:** Excitation temperature map of  $^{13}\text{CO}$

### 4.2.3 Velocity Distribution

Modelling the line also provides the estimate of velocity at which line is centered, which can give insights about the velocity gradient of the gas in different regions of the cloud. Right panel of Fig 4.7 shows the LSR velocity map of  $^{13}\text{CO}$ , a velocity gradient of  $0.5\text{--}1.0 \text{ km s}^{-1}$  can be seen while going from lower to higher declination. However since the significance of the observed velocity gradient needs further study, especially using maps of  $^{12}\text{CO}$  since  $^{12}\text{CO}$  is the best tracer of the overall gas distribution in the cloud.

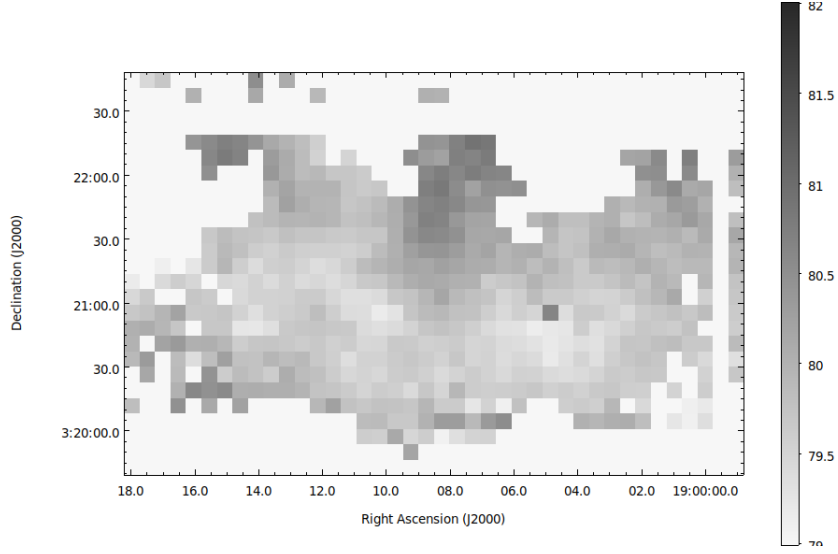


**Figure 4.7:** Velocity wrt LSR map of  $^{13}\text{CO}$

#### 4.2.4 Isotopic Ratio

Lower Abundance ratio were observed from modelling  $^{13}\text{CO}$  with  $\text{C}^{18}\text{O} \approx$  ranges from 3-8 as shown in Fig. 4.8. While generally observed abundance ratio is 6-10 (Wilson and Rood, 1994). Lower abundance ratios has been also observed in dense region due to dependency of  $X(^{13}\text{CO}/\text{C}^{18}\text{O})$  on galactocentric distance (Wilson and Rood, 1994) and also on the physical conditions of the region. For example (Paron et al., 2018) observed the abundance ratios in variety of interstellar environment and using the LTE Analysis found that average value of abundance ratio is 5, varying from 1.5 to 10.5.

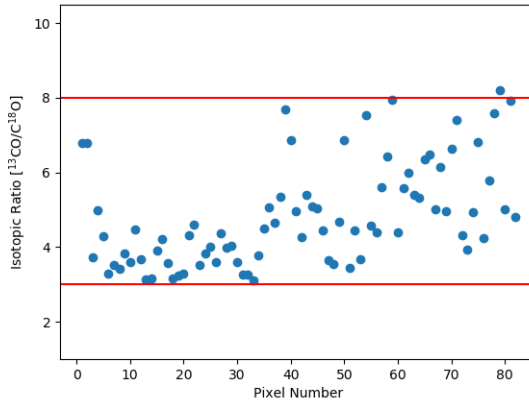


**Figure 4.8:** Observed isotopic ratio  $[^{13}\text{CO}/\text{C}^{18}\text{O}]$

## Chapter 5

# Future Work

Estimation of several physical parameters has been done for molecules like  $^{12}\text{CO}$ ,  $^{13}\text{CO}$  and  $\text{C}^{18}\text{O}$ . Further analysis is required to derive clump radius, mass, virial ratio etc which will provide more deeper insights about their physical properties. Outflows from the core has been detected, corresponding outflow properties such as velocity, momentum, energy etc need to be estimated, which will provides information related to mass accretion. Complimentary ATLASGAL 870, 350, 250, 160  $\mu\text{m}$  dust emission data is available for the studied source. Estimation of dust temperature and column density need to be carried out as discussed for one pixel in section 3.3, using SED fitting. Then dust temperature can be compared with excitation temperature to whether both are equal or different.

CO is considered as low dense gas tracer as its critical density is low. So to study the denser region higher critical density molecules data is also available for the studied source. So  $\text{HCO}^+$ ,  $\text{H}^{13}\text{CO}^+$ , HCN and  $\text{N}_2\text{H}^+$  also have to be modelled as they traces different properties of the region and their corresponding maps need to be generated. A proper correlation from the different molecular transitions need to set up and the detailed physical properties such as internal heating, prominent velocity gradient, infall motion etc need to be studied. Till now have studied just one source, if time permits 10 such sources need to be studied as mentioned in introduction. Their maps of several parameters like temperature, density etc same as that done for the first source need to be made. And comparison with the theoretical models will be drawn which will provide more constraints for the high mass star formation theory.

# Bibliography

Afonso, J. M., J. L. Yun, and D. P. Clemens

1998. Hcn in bok globules: a good tracer of collapsing cores. *The Astronomical Journal*, 115(3):1111.

Carey, S., A. Noriega-Crespo, D. Mizuno, S. Shenoy, R. Paladini, K. Kraemer, S. Price, N. Flagey, E. Ryan, J. Ingalls, et al.

2009. Mipsgal: A survey of the inner galactic plane at 24 and 70  $\mu\text{m}$ . *Publications of the Astronomical Society of the Pacific*, 121(875):76.

Caselli, P., P. J. Benson, P. C. Myers, and M. Tafalla

2002. Dense cores in dark clouds. xiv. n2h+ (1-0) maps of dense cloud cores. *The Astrophysical Journal*, 572(1):238.

Dickman, R. L.

1976. Ratio of carbon monoxide to molecular hydrogen in interstellar dark clouds.

Girart, J. M., P. T. Ho, A. L. Rudolph, R. Estalella, D. J. Wilner, and L. M. Chernin

1999. The hco+ molecular outflow in ngc 2071. *The Astrophysical Journal*, 522(2):921.

Goicoechea, J. R., M. G. Santa-Maria, E. Bron, D. Teyssier, N. Marcelino, J. Cernicharo, and S. Cuadrado

2019. Molecular tracers of radiative feedback in orion (omc-1)-widespread ch+ (j=1-0), co (10-9), hcn (6-5), and hco+ (6-5) emission. *Astronomy & Astrophysics*, 622:A91.

Goldsmith, P. F.

1972. Collisional excitation of carbon monoxide in interstellar clouds. *The Astrophysical Journal*, 176:597.

Goldsmith, P. F.

1999. Probing molecular clouds—their density and structure. In *Millimeter-Wave Astronomy: Molecular Chemistry & Physics in Space*, Pp. 57–94. Springer.

Goldsmith, P. F. and W. D. Langer

1999. Population diagram analysis of molecular line emission. *The Astrophysical Journal*, 517(1):209.

Klessen, R. S.

2011. Star formation in molecular clouds. *EAS Publications Series*, 51:133–167.

Krumholz, M. R.

2011. Star formation in molecular clouds. In *AIP Conference Proceedings*, volume 1386, Pp. 9–57. AIP.

Lee, S. H., Y.-S. Park, J. Sohn, C. W. Lee, and H. M. Lee

2007. Velocity distribution of collapsing starless cores, 1694-2 and 11197. *The Astrophysical Journal*, 660(2):1326.

Liu, X.-L., J.-J. Wang, and J.-L. Xu

2014. Physical properties, kinematics and mass function of 12 northern infrared dark clouds. *Monthly Notices of the Royal Astronomical Society*, 443(3):2264–2284.

Milam, S., C. Savage, M. Brewster, L. M. Ziurys, and S. Wyckoff

2005. The  $^{12}\text{C}/^{13}\text{C}$  isotope gradient derived from millimeter transitions of  $\text{CN}$ : The case for galactic chemical evolution. *The Astrophysical Journal*, 634(2):1126.

Nakamura, F., S. Oyamada, S. Okumura, S. Ishii, Y. Shimajiri, Y. Tanabe, T. Tsukagoshi, R. Kawabe, M. Momose, Y. Urasawa, et al.

2019. Nobeyama 45-m mapping observations toward orion a. iii. multi-line observations toward an outflow-shocked region, omc-2 fir. *arXiv preprint arXiv:1906.11454*.

Ossenkopf, V. and T. Henning

1994. Dust opacities for protostellar cores. *Astronomy and Astrophysics*, 291:943–959.

Padoan, P., M. Juvela, J. Bally, and Å. Nordlund

1997. A theoretical calibration of  $\hat{\{^{13}\text{C}\}}$  column density in molecular clouds. *arXiv preprint astro-ph/9706177*.

- Paron, S., M. B. Areal, and M. E. Ortega  
2018. Mapping the  $^{13}\text{CO}/^{18}\text{O}$  abundance ratio in the massive star-forming region g29.96-0.02. *Astronomy & Astrophysics*, 617:A14.
- Phillips, T., P. Huggins, P. Wannier, and N. Scoville  
1979. Observations of  $\text{CO}(J=2-1)$  emission from molecular clouds. *The Astrophysical Journal*, 231:720–731.
- Polychroni, D., T. J. Moore, and J. Allsopp  
2012. The gas properties of the w3 giant molecular cloud: a harp study. *Monthly Notices of the Royal Astronomical Society*, 422(4):2992–3003.
- Rigby, A., T. Moore, R. Plume, D. Eden, J. Urquhart, M. Thompson, J. Mottram, C. Brunt, H. Butner, J. Dempsey, et al.  
2015. Chimps: the  $^{13}\text{CO}/^{18}\text{O}$  ( $J=3-2$ ) heterodyne inner milky way plane survey. *Monthly Notices of the Royal Astronomical Society*, 456(3):2885–2899.
- Schuller, F., K. Menten, Y. Contreras, F. Wyrowski, P. Schilke, L. Bronfman, T. Hennig, C. Walmsley, H. Beuther, S. Bontemps, et al.  
2009. Atlasgal—the apex telescope large area survey of the galaxy at 870  $\mu\text{m}$ . *Astronomy & Astrophysics*, 504(2) : 415 – 427.
- Scoville, N. Z.  
2012. Evolution of star formation and gas. *arXiv preprint arXiv:1210.6990*.
- Shimoikura, T., K. Dobashi, F. Nakamura, C. Hara, T. Tanaka, Y. Shimajiri, K. Sugitani, and R. Kawabe  
2015. Dense clumps and candidates for molecular outflows in w40. *The Astrophysical Journal*, 806(2):201.
- Van der Tak, F., J. H. Black, F. Schöier, D. Jansen, and E. F. van Dishoeck  
2007. A computer program for fast non-lte analysis of interstellar line spectra—with diagnostic plots to interpret observed line intensity ratios. *Astronomy & Astrophysics*, 468(2):627–635.

Wilson, T. and R. Rood

1994. Abundances in the interstellar medium. *Annual Review of Astronomy and Astrophysics*, 32(1):191–226.